Simulations of Cavitating Flows in Turbopumps

A. Hosangadi,* V. Ahuja,† and R. J. Ungewitter†
Combustion Research and Flow Technology, Inc., Pipersville, Pennsylvania 18947

Simulations of a cavitating inducer at design flow conditions are reported in this paper. The ability of a Navier–Stokes based, multiphase formulation in modeling the effects of large-scale extensive cavitation on the performance of inducers is demonstrated. The simulations were performed on the Simplex inducer geometry that has been extensively tested at NASA Marshall Space Flight Center. An acoustically accurate, compressible multiphase model that has been previously validated is utilized. The model is implemented within a multi-element unstructured framework that permits efficient grids with locally high resolution near the cavitating zones and in the tip gap region. The simulations were performed at a fixed flow rate with different inflow pressures or net suction specific speeds (N_{SS}). The computational analysis indicates a strong correlation between performance loss and the extent of cavitation blockage and accurately identifies the critical N_{SS} number where breakdown occurs. Predictions of head loss compare well with experimental data. Key insights are provided through a sequence of relevant simulations into the growth of cavitation zones, blockage in blade passages, and change in blade loading as a result of cavitation.

Nomenclature

Cav.No.	=	$(p_\infty - p_v)/\frac{1}{2}\rho_\infty Q_\infty^2$
c_m, c_g, c_L	=	speed of sound in mixture, gas, liquid
D_v	=	viscous flux vector
E, F, G	=	flux vectors
K_f, K_b	=	rate constants for vapor and liquid formation
k, ε	=	turbulent kinetic energy, turbulent dissipation rate
N	=	rotational speed, rpm
N_{ss}	=	net suction specific speed
p	=	pressure
p_v	=	$p_\infty - \frac{1}{2}\rho_\infty Q_\infty^2 * $ Cav.No.
Q	=	vector of conservative variables
Q_f	=	flow rate, gallons per minute (gpm)
Q_v	=	vector of primative variables
S	=	source terms vector
S_g	=	cavitation source term
u, v, w	=	x, y, z components of velocity
Γ	=	preconditioning matrix
ρ_m, ρ_g, ρ_L	=	density of mixture, gas, liquid
τ_b	=	time constant for liquid reconversion
τ_f	=	time constant for vapor formation
$\phi_g \phi_L$	=	void fraction of gas, liquid

Introduction

TURBOPUMPS associated with feed systems in space applications operate at high rotational speeds, thereby permitting a substantial reduction in weight and size. However, high rotational speeds make these systems susceptible to cavitation. This is particularly true for inducers, which operate at low fluid pressures that are close to the vapor pressure. Cavitation effects lead to a breakdown of head generation at high suction specific speeds. The head breakdown is typically rapid and occurs at a critical value of suction specific speed. Furthermore, the critical breakdown value can be significantly lower at off-design conditions. Therefore, identifying the critical breakdown value is a key parameter in the design process and is used to identify safe operation regimes for the system. However, detailed computational-fluid-dynamics (CFD) analyses of cavitating pump systems are seldom used for design and performance predictions. This is at least partly because numerical models have not been shown to be sufficiently accurate and robust to be used in a routine manner under extensive cavitation conditions. However, because turbopump designs for future space systems are being required to throttle over a wide range of off-design conditions, where dynamic pressure fluctuations resulting from coupling between cavitation and hydrodynamics become dominant, it becomes essential to develop more sophisticated and reliable CFD tools that can aid the design process.

The development of numerical models to simulate cavitating flows has continued to receive attention from a broad range of research groups. For the purposes of our discussion here, cavitation models in CFD tools can broadly be classified into two categories: 1) a bubbly framework using the Rayleigh–Plesset equation and 2) continuum formulation solving for gas-phase transport. We note in this section that no distinction is made between noncondensable gas and vapor when referring to gas volume and mass fractions. There have been numerous numerical studies using the bubbly closure model (e.g., Refs. 1 and 2). Here, the flowfield is seeded with bubbles, and the change in bubble mass (and therefore the mixture density in each cell) is obtained from the Rayleigh–Plesset equations. The advantage of this formulation is that a physical model describes the cavitation phase change. However, the key limitation of these studies arises from their implicit restriction that the mixture be "dilute," that is, the gas void fraction be negligibly small. For instance, Kubota et al.[1] define mixture density as $\rho_m = (1 - \phi_g)\rho_l$, which neglects the vapor phase. When $\phi_g \approx 1$, the conservation equations for the mixture become singular. This is a severe restriction. In particular, for cloud cavitation problems where the vapor clouds are very dense and the spatial extent of each distinct cloud can be large, the flowfield within the gas phase has to be resolved numerically.

The second approach followed is a continuum formulation that is applicable to dense cavitating flow (e.g., Refs. 3–6). Here, a separate equation for the transport of the gas phase is solved for, and there is no restriction on the volume fraction of the gas phase being small. The cavitation process is modeled as a phase-change source term. Cavitation is typically modeled with a rate equation for phase change based on the local pressure. Although the works just referenced use different formulations to specify this rate of phase change, they are similar in that they do not integrate the cloud bubble dynamics because neither the radius nor the number density of the bubbles in the vapor cloud are computed. In general, good results are obtained for the mean cavitation solutions. We note that this is

*Principal Scientist; hosangad@craft-tech.com. Senior Member AIAA.
†Research Scientist. Senior Member AIAA.

also the cavitation phase-change model used in the present study. However, for unsteady cloud cavitation the development of more rigorous unsteady cavitation models will be necessary.

For turbomachinery simulations, CFD technology is currently limited to simulating mean cavitating performance at design conditions for idealized liquids (no thermodynamic effects). Typical simulations show comparisons with data at design conditions for the head coefficient and the critical N_{SS} number at which performance breakdown occurs.[7-10] However flows at off-design conditions, where large-scale unsteadiness and high dynamic pressure loads are observed, cannot at this point be reliably predicted; cavitation instabilities and rotational cavitation modes in pumps have not been simulated by any group to the best of our knowledge. Thus, to develop a CFD simulation framework that can eventually simulate unsteady, off-design performance of liquid rocket turbopumps, significant development will be required from the current level of technology.

The numerical model employed for the inducer simulations presented here is an acoustically accurate form of the compressible multiphase equation system developed earlier by the authors.[5] The equation system is cast in a time-marching framework by relating the local speed of sound in the two-phase mixture to the local void fraction and the individual phase acoustic speeds. We note that the system presented here is closed and does not require additional equations to resolve the gas/liquid interface. The phase change during the cavitation process is modeled using finite-rate source terms. Details of the numerical formulation and the phase-change source term are provided in the following sections.

The numerical code utilized in our simulations is the CRUNCH CFD® code, which is a multi-element-based unstructured code.[11-13] The underlying philosophy in the CRUNCH CFD code is to tailor the grid topology to resolving the dominant flow phenomena and the structural complexity of the problem. This is achieved by utilizing a combination of hexahedral, tetrahedral, prismatic, and pyramidal elements in mesh construction. Such a framework is particularly attractive for complex turbomachine configurations because it provides the flexibility of generating high quality grids with minimum skewness. Furthermore, the ability to perform local grid adaption aids in generating high grid resolution locally in the vicinity of the cavitation zone. For efficient computations of large three dimensional problems, a parallel framework for distributed memory systems has been implemented.

Simulation results are presented for the cavitating performance of the Simplex inducer at its design flow rate at various N_{SS} numbers. The Simplex inducer Bordelon et al.[14] is a three-bladed geometry that has been instrumented heavily and has undergone extensive water testing at NASA Marshall Space Flight Center. A detailed analysis of the breakdown characteristics is provided in the Results section along with physical correlations between performance and cavitation blockage.

Multiphase Equation System

The multiphase equation system is written in vector form as

$$\frac{\partial \boldsymbol{Q}}{\partial t} + \frac{\partial \boldsymbol{E}}{\partial x} + \frac{\partial \boldsymbol{F}}{\partial y} + \frac{\partial \boldsymbol{G}}{\partial z} = \boldsymbol{S} + \boldsymbol{D}_v \tag{1}$$

Here $\boldsymbol{Q}$ is the vector of dependent variables. The viscous fluxes are given by the standard full compressible form of Navier–Stokes equations. The vectors $\boldsymbol{Q}$, $\boldsymbol{E}$, and $\boldsymbol{S}$ are given next with a detailed discussion on the details of the cavitation source terms to follow later:

$$\boldsymbol{Q} = \begin{pmatrix} \rho_m \\ \rho_m u \\ \rho_m v \\ \rho_m w \\ \rho_g \phi_g \\ \rho_m k \\ \rho_m \varepsilon \end{pmatrix} \quad \boldsymbol{E} = \begin{pmatrix} \rho_m u \\ \rho_m u^2 + P \\ \rho_m u v \\ \rho_m u w \\ \rho_g \phi_g u \\ \rho_m k u \\ \rho_m \varepsilon u \end{pmatrix} \quad \boldsymbol{S} = \begin{pmatrix} 0 \\ 0 \\ 0 \\ 0 \\ S_g \\ S_k \\ S_\varepsilon \end{pmatrix} \tag{2}$$

For now in Eq. (2), the energy equation has been dropped because each phase is assumed to be nearly incompressible thereby decoupling the pressure work term. For cryogenic working fluids, an additional scalar equation for mixture enthalpy would be solved coupled to this equation because temperature effects become important. The mixture density and gas porosity are related by the following relations locally in a given cell volume:

$$\rho_m = \rho_g \phi_g + \rho_L \phi_L \tag{3}$$

$$1 = \phi_g + \phi_L \tag{4}$$

To modify the system in Eq. (1) to a well-conditioned form in the incompressible regime, a two-step process is required: an acoustically accurate two-phase form of Eq. (1) is first derived, followed by a second step of time scaling or preconditioning to obtain a well-conditioned system. We begin by defining the acoustic form of density differential for the individual gas and liquid phase as follows:

$$\mathrm{d}\rho_g = \left(1/c_g^2\right)\mathrm{d}P, \qquad \mathrm{d}\rho_l = \left(1/c_L^2\right)\mathrm{d}P \tag{5}$$

Here c_g is the isothermal speed of sound $(\partial P/\partial \rho_g)_T$ in the pure gas phase and c_L is the corresponding isothermal speed of sound in the liquid phase, which is a finite value. The differential form of the mixture density ρ_m is obtained by differentiating Eq. (3) and using the relationship given in Eq. (5) to obtain

$$\mathrm{d}\rho_m = (\rho_g - \rho_L)\,\mathrm{d}\phi_g + \left(1/c_\phi^2\right)\mathrm{d}P$$

$$\left(1/c_\phi^2 = \phi_g/c_g^2 + \phi_L/c_L^2\right) \tag{6}$$

Here, c_ϕ is a variable defined for convenience and is not the acoustic speed c_m in the mixture, which will be defined later. Using Eq. (6), Eq. (1) can be rewritten as

$$\Gamma\frac{\partial \boldsymbol{Q}_v}{\partial t} + \frac{\partial \boldsymbol{E}}{\partial x} + \frac{\partial \boldsymbol{F}}{\partial y} + \frac{\partial \boldsymbol{G}}{\partial z} = S + \boldsymbol{D}_v \tag{7}$$

and

$$\boldsymbol{Q}_v = [p, u, v, w, \phi_g, k, \varepsilon]^T \tag{8}$$

The numerical characteristics of Eq. (7) are studied by obtaining the eigenvalues of the matrix, $[\Gamma^{-1}(\partial E/\partial Q_v)]$. The eigenvalues of the system are derived to be

$$\Lambda = (u + c_m, u - c_m, u, u, u, u, u) \tag{9}$$

where c_m turns out to be the well-known, harmonic expression for the speed of sound in a two-phase mixture and is given as

$$1/c_m^2 = \rho_m\left[\phi_g/\rho_g c_g^2 + \phi_L/\rho_L c_L^2\right] \tag{10}$$
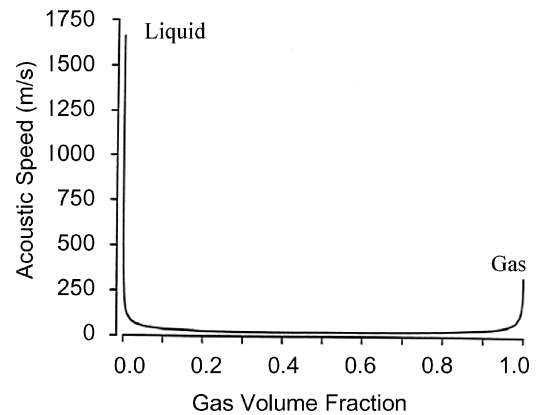

Fig. 1   Speed of sound in a two-phase gas-liquid mixture.

The behavior of the two-phase speed of sound is plotted in Fig. 1 as a function of the gas porosity; at either limit the pure single-phase acoustic speed is recovered. However, away from the single-phase limits the acoustic speed rapidly drops below either limit value and remains at the low level in most of the mixture regime. As a consequence, the local Mach number in the interface region can be large even in low-speed flows.

We reemphasize a critical observation at this point: the equation system (7–9) is completely defined and does not require ad hoc closure models for the variation of mixture density with pressure. In that respect alone this represents a significant advancement over most other cavitation models in the literature. The acoustic speeds for individual phases are well-defined physical quantities, which can be specified, and so is the case with physical material densities (ρ_g, ρ_L) for each individual phase. For low-pressure incompressible regimes, the material densities can be assumed to be constant without significant error in the solutions. However, in its most general form the material densities for each phase can be obtained from the pressure using their respective physical equations of state (e.g., ideal-gas law for gases, etc.) if that is so desired. If temperature variations were significant, this would involve solving an additional equation for the mixture energy.[15]

To obtain an efficient time-marching numerical scheme, preconditioning is now applied to the system in Eq. (7), in order to rescale the eigenvalues of the system so that the acoustic speeds are of the same order of magnitude as the local convective velocities.[5]

Cavitation Source Terms

In the present effort, the cavitation source term is defined via a simplified nonequilibrium, finite-rate form as follows:

$$S_g = K_f \rho_L \phi_L + K_b \rho_g \phi_g \qquad (11)$$

where the constant K_f is the rate constant for vapor being generated from liquid in a region where the local pressure is less than the vapor pressure. Conversely, K_b is the rate constant for reconversion of vapor back to liquid in regions where the pressure exceeds the vapor pressure. Here, the rate constants are specified using the form given by Ref. 16:

$$K_b = \begin{bmatrix} 0 & p < p_v \\ \dfrac{1}{\tau_b}\left(\dfrac{Q_\infty}{L_\infty}\right) & \left[\dfrac{p-p_v}{\frac{1}{2}\rho_\infty Q_\infty^2}\right] & p > p_v \end{bmatrix}$$

$$K_f = \begin{bmatrix} 0 & p > p_v \\ \dfrac{1}{\tau_f}\left(\dfrac{Q_\infty}{L_\infty}\right) & \left[\dfrac{p-p_v}{\frac{1}{2}\rho_\infty Q_\infty^2}\right] & p < p_v \end{bmatrix} \qquad (12)$$

We note that the nonequilibrium timescales have not been correlated with experimental data. For steady attached cavitation this simplified form might be adequate because the cavitation timescales do not interact with the fluid timescales if the cavitation rate constants are fast enough. This point has been discussed in detail in our earlier work,[5] where we demonstrate the insensitivity of the solution to the rate by repeating a calculation for a given cavitation number at three different rates. We note that in the present study the baseline vaporization and condensation rate parameters were set at 0.01 s. For unsteady cavitation, however, the details of how the nonequilibrium source term is specified could be crucial because it might couple with transient pressure waves. The development of a more rigorous nonequilibrium source term model is a topic of ongoing research.

Turbulence Models

The standard high-Reynolds-number form of the $k-\varepsilon$ equations form the basis for all turbulence modeling in CRUNCH CFD. Transport equations for the turbulent kinetic energy and its dissipation rate are solved along with the basic momentum and energy equations.

These equations, with supplemental low-Reynolds-number terms, are as follows:

$$\frac{\partial \rho k}{\partial t} + \frac{\partial}{\partial x_i}\left[\rho u_i k - \left(\mu + \frac{\mu_T}{\sigma_k}\right)\frac{\partial k}{\partial x_i}\right] = P_k - \rho\varepsilon + S_k$$

$$\frac{\partial \rho \varepsilon}{\partial t} + \frac{\partial}{\partial x_i}\left[\rho u_i \varepsilon - \left(\mu + \frac{\mu_T}{\sigma_\varepsilon}\right)\frac{\partial \varepsilon}{\partial x_i}\right] = C_1 f_1 P_k - C_2 f_2 \rho\varepsilon + S_\varepsilon$$

$$P_k = \tau_{ij}\frac{\partial u_i}{\partial x_j}, \qquad \tau_{ij} = -\frac{2}{3}\rho k + 2\mu_T * \left(S_{ij} - \frac{1}{3}\frac{\partial u_k}{\partial x_k}\delta_{ij}\right)$$

$$\mu_T = C_\mu f_\mu \rho \frac{k^2}{\varepsilon} \qquad (13)$$

where σ_k, σ_ε, C_1, and C_2 are the modeling constants, and f_1, f_2, f_μ are empirical modeling functions to account for low Reynolds number (near wall). (They equal unity in the high-Reynolds-number form.)

Low-Reynolds-number effects in the near wall are accounted for by using an extension of the near-wall model of So et al.[17] This model has been shown to reproduce the near-wall asymptotic relations for the Reynolds stress and kinetic energy accurately. In this model, the damping functions f_1, f_2, f_μ, are defined as follows:

$$f_1 = 1.0 - \exp\left[-\left(\frac{Re_t}{40}\right)^2\right]$$

$$f_2 = 1 - \frac{2}{9}\exp\left[-\left(\frac{Re_t}{6}\right)^2\right]$$

$$S_\varepsilon = \frac{1}{4}c_3\mu_L\left[\left(\frac{\partial k^{\frac{1}{2}}}{\partial x}\right)^2 + \left(\frac{\partial k^{\frac{1}{2}}}{\partial y}\right)^2 + \left(\frac{\partial k^{\frac{1}{2}}}{\partial z}\right)^2\right] \qquad (14)$$

where

$$Re_t = \rho k^2 / \mu_L \varepsilon$$

$$f_\mu = \left(1 + 4Re_t^{-\frac{3}{4}}\right)\tanh(Re_k/125)$$

where

$$Re_k = \rho\sqrt{k}\,y / \mu$$

The constants for this model are given as follows:

$$c_\mu = 0.09, \qquad \sigma_k = 1.4, \qquad \sigma_\varepsilon = 1.4$$
$$c_1 = 1.44, \qquad c_2 = 1.92, \qquad c_3 = 2.9556 \qquad (15)$$

This model has been tested for a number of standard turbulence test cases to verify that it gives correct boundary-layer growth and reattachment length for recirculating flows. For cavitating flows, where large density gradients are present as a result of multifluid composition, the rigorous validation of the turbulence model will require further study; however, this is beyond the scope of the present paper. However, results for a headform geometry presented in our earlier paper[5] indicate that the turbulence model performs adequately and provides correct mean pressure variation.
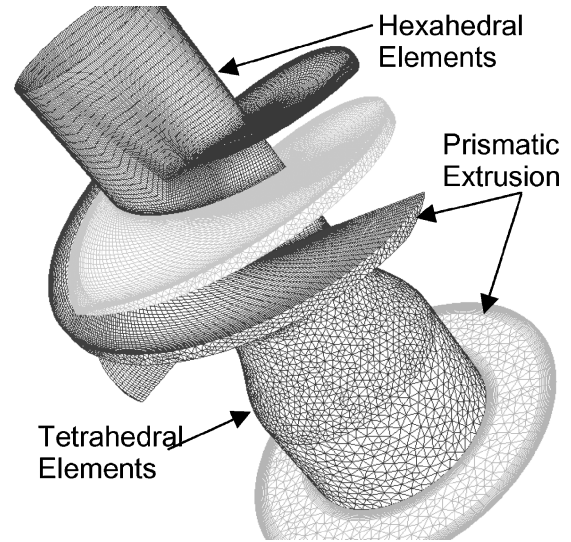
Results and Discussion

The inducer configuration chosen for our present numerical study is the Simplex inducer that has been designed and tested extensively

Table 1 Detailed calculations performed for simplex inducer at various N_{SS} numbers at design flow rate

With tip gap	No tip gap (rotating shroud)
Baseline (single phase): 5,000	Baseline (single phase)
Before breakdown: 16,700	Before breakdown: 16,700
Breakdown range: 18,500, 19,780, 20,258	———
Postbreakdown: 20,700, 25,700	Postbreakdown: 20,700, 25,700

a) Inlet view

b) Side view

c) Blade angle distortion
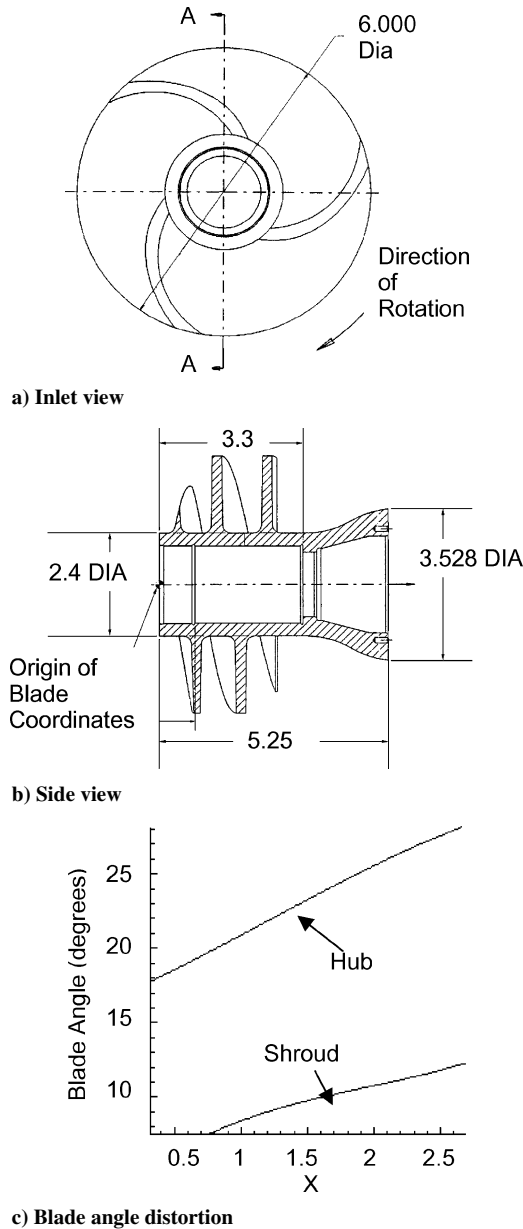
Fig. 2 Geometry for three-bladed simplex inducer (taken from Bordelon et al.[14]).

Fig. 3 Multi-element grid for inducer.

at NASA Marshall Space Flight Center.[14] This inducer has a three-bladed geometry (see Figs. 2a and 2b) with blade tip diameter of 6 in. [0.1404 m], a hub diameter of 2.4 in. [0.05616 m], and a tip-gap clearance of 0.03 in. [0.702 mm] between the blade and the shroud. The variation of blade angle at both the tip and the hub with axial distance are also shown in Fig. 2c. The design rpm is 5000 at a flow rate of 909 gpm with an inlet tip flow coefficient of 0.094. The Reynolds number based on the axial velocity is $1.09263E+05$ for a water temperature of 80°F. The inlet static pressure can be varied from 3–30 psia to obtain N_{SS} numbers in the range of 0–30,000. All of the calculations presented here were done at the design flow rate at different inlet pressures, that is, the N_{SS} number was

varied past the head breakdown value. The N_{SS} number is defined as $N_{ss} = [N \times \sqrt{(Q_f)}]/(NPSH)^{3/4}$. Here, N is the rotational speed in rpm, Q_f is the flow rate in gpm, and $NPSH$ is the inflow suction head in feet.

The multi-element unstructured grid generated for the simplex inducer is shown in Fig. 3. The region between the blades was generated using hexahedral blocks. This was done to ensure good resolution at the leading edge of the blade where the cavity forms and where the largest gradients in density are present. The grid blocks between the pressure and suction side were staggered to reduce skewness in the grid blocks. Thus even though the grid points are contiguous across the pressure and suction side a structured block in the tip-gap region is cumbersome. An alternate solution is to exploit the multi-element feature by triangulating the top surface of the blade and extruding prisms in the tip-gap region over the extent of the blade thickness; this resulted in a grid for the tip gap with relatively no skewness. The region downstream of the blades was gridded with prismatic/tetrahedral cells. This was done primarily to reduce the size of the overall grid, thereby maintaining a workable size grid. Hexahedral cells would entail carrying the grid resolution across the radial cross section substantially increasing the grid size. In contrast, tetrahedral cells are very efficient in gridding up large volumes with nearly isotropic cells making the grid very compact. The multi-element grid shown here for the complete three-dimensional geometry had approximately two million cells and the simulations were carried out on 32 processors of a linux PC-cluster. Thus an optimal grid was generated for the geometry by tailoring the cell topology to the requirements of the problem.

A substantial number of simulations at various N_{SS} numbers were carried out to evaluate the ability of the numerical formulation to predict the performance characteristic of the inducer (see Table 1). At the design flow rate, the critical N_{SS} number at which the head coefficient shows a sudden drop is approximately 18,000–20,000. As Table 1 shows, a significant number of calculations were performed around this value to ascertain if the present formulation can pick up the change in the flowfield characteristic. Figure 4 shows the pressure contours on the hub as well as on the blades for a single-phase (baseline) simulation where cavitation was suppressed
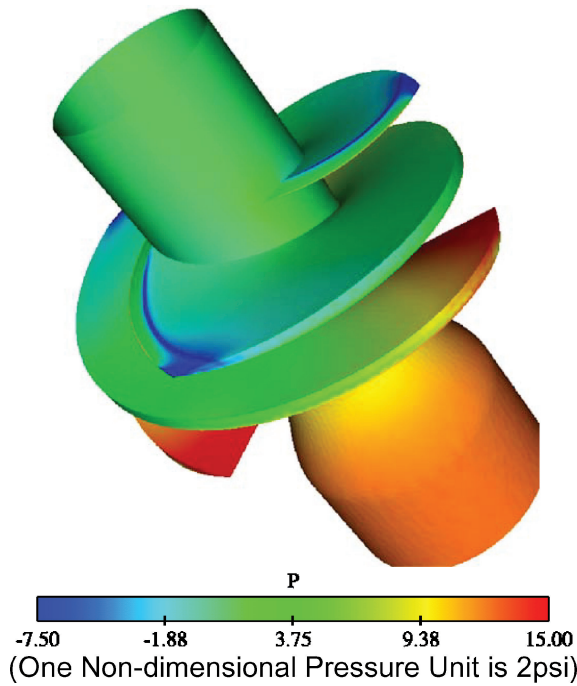
P

-7.50   -1.88   3.75   9.38   15.00

(One Non-dimensional Pressure Unit is 2psi)

Fig. 4   Pressure distribution on inducer blades at N_{SS} number 5000 (single phase).

N_{ss} = 16, 700 N_{ss} = 20, 700 N_{ss} = 25, 700

P

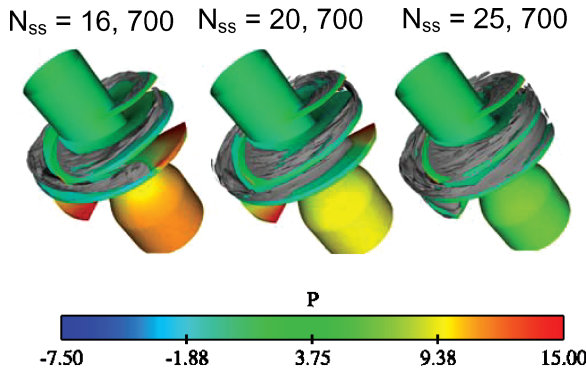-7.50   -1.88   3.75   9.38   15.00

Fig. 5   Pressure distribution and gas void fraction isosurface (0.5) for N_{SS} numbers 16,700, 20,700 and 25,700.

by specifying an artificially high cavitation number. We note that an extremely low-pressure region is observed along the leading edge of the blade and particularly near the junction of the tip and the shroud where this low-pressure region also generates reverse flow. For the cavitating cases, this low-pressure region is the initial source of vapor generation. However, as we shall discuss next, the generation of vapor leads to substantial changes in the flow streamlines raising the pressure on the leading edge and pushing the initial cavitation downstream to the bend where the blade goes to its full thickness. We note that the flowfield contours shown here are instantaneous contours in the rotating frame of reference.

The corresponding pressure contours on the blade are shown for N_{SS} numbers of 16,700, 20,700, and 25,700 in Fig. 5 along with the isosurface for the cavitation zone. As just discussed, we observe that the cavitation zone is attached to the bend in the blade where the blade profile goes to its full thickness. The second observation we make is that the cavitation zone in the tip-gap region itself is spotty with the main cavitation zone ending slightly below the tip of the blade. This could partly be cause by the relatively large value of the tip gap, which results in a very energetic flow with large turbulence intensity leaking through from the pressure side to the suction side. Particle streamlines shown in Fig. 6 indicate that reverse velocity in the tip gap is high enough to cause the fluid crossing over to go back all of the way upstream of the blade leading edge before slowing
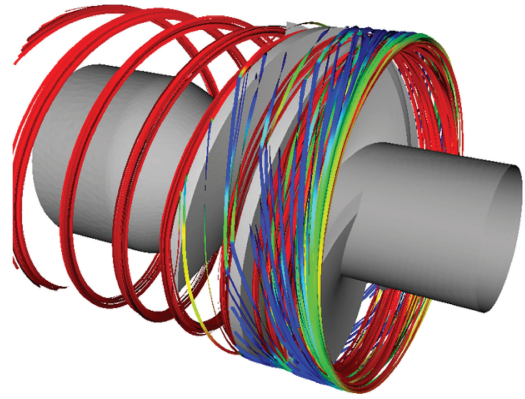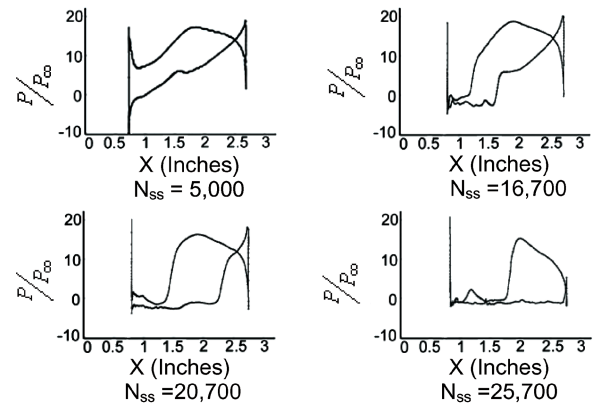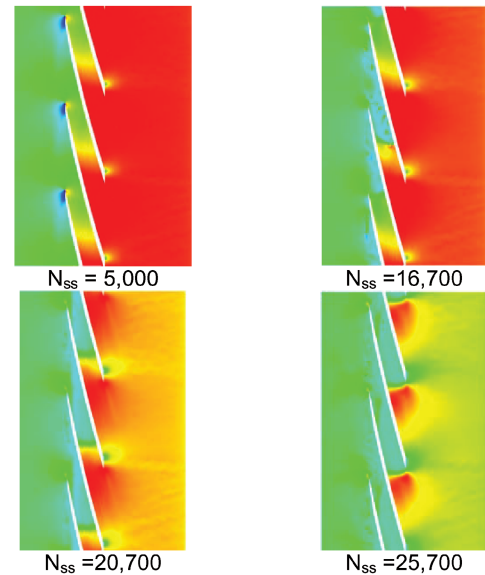

Fig. 6   Streamlines indicating flow in tip-gap region.

a) Pressure profiles on blade surface

b) Pressure contours

P

-7.50   -1.88   3.75   9.38   15.00

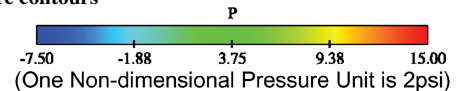(One Non-dimensional Pressure Unit is 2psi)

Fig. 7   Pressure distribution at radius = 2.9 in.

down and turning around again. As the N_{SS} number increases, the cavitation zone extends further downstream and gets much thicker in the cross-sectional plane. In our discussion to follow, we shall examine the extent of the cavitation zone at various radial cross-sectional cuts to try and better understand the reason for the head loss.

The pressure contours and blade loadings at a radius of 2.9 in. (just below the tip) are shown in Fig. 7, with the similar plots for the
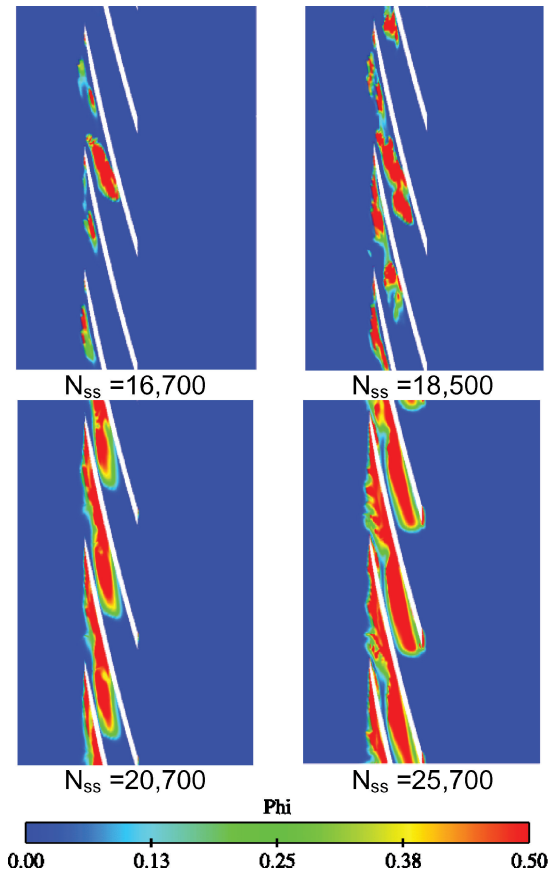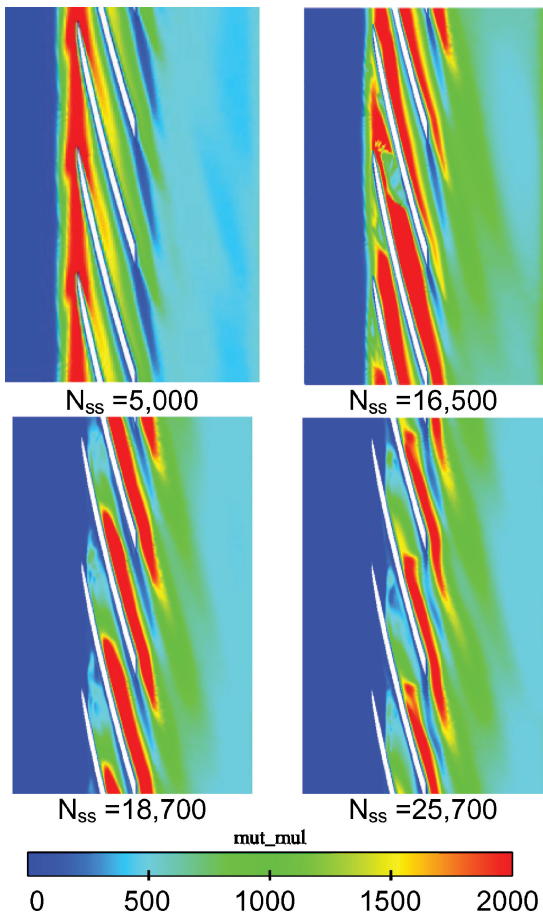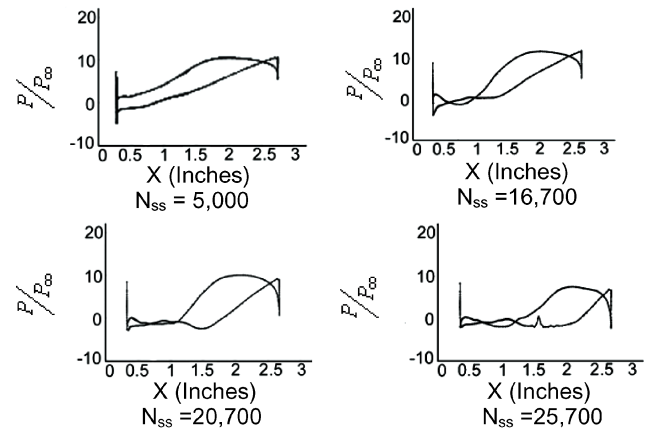
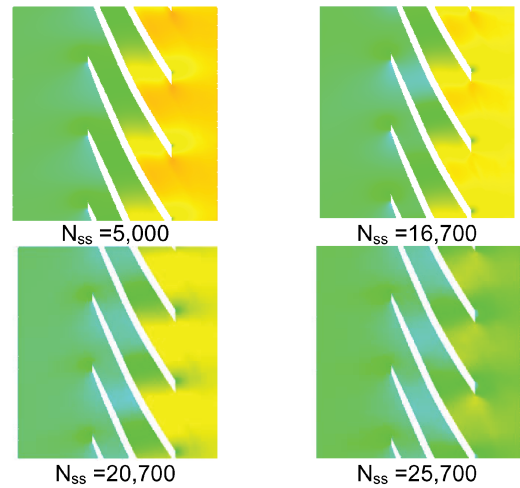Fig. 8 Gas void fraction at radius = 2.9 in.

Fig. 9 Turbulent viscosity distribution at radius = 2.9 in.

a) Pressure profiles on blade surface

b) Pressure contours

(One Non-dimensional Pressure Unit is 2psi).

Fig. 10 Pressure distribution at radius = 1.3 in.

gas volume fraction and turbulent viscosity (which is obtained from the turbulent kinetic energy and dissipation) shown in Figs. 8 and 9, respectively. The pressure profiles on the blade clearly demarcate the extent of the cavitation zone. The axial extent of the cavitation zone increases at larger N_{SS} numbers with the entire suction surface being covered by gas at an N_{SS} number of 25,700. In fact, at this N_{SS} number the only part of the pressure side that generates head is the portion that extends beyond the influence zone of the suction side of the neighboring blade. The pressure in the cavitation zone is close to the vapor pressure; at larger N_{SS} numbers the vapor pressure is larger when normalized by the inflow pressure value, and the blade loading plots reflect this. An examination of the cavitation zone in Fig. 8 reveals that at the N_{SS} number of 21,000, the cavitation zone covers the entire region between the pressure and suction side.

The complete blockage that results near the shroud forces the flow to turn and go around the blockage, resulting in substantial viscous losses and corresponding sharp losses in the head coefficient. The turbulent viscosity contours shown in Fig. 9 indicate significant turbulence growth on the pressure side. As cavitation sets in, turbulent viscosity levels in the cavitation zone drop significantly because of the density change (i.e., the gas density is much lighter than the liquid resulting in lower local Reynolds numbers).

The corresponding flowfield contours closer to the hub at a radius of 1.3 in. are shown in Figs. 10–12. The pressure loading on the blade indicates that as cavitation sets in the loading on the pressure and suction side reverse with the pressure being higher on the suction side. Interestingly, the turbulent viscosities also show a different feature with turbulence growth being more pronounced on the
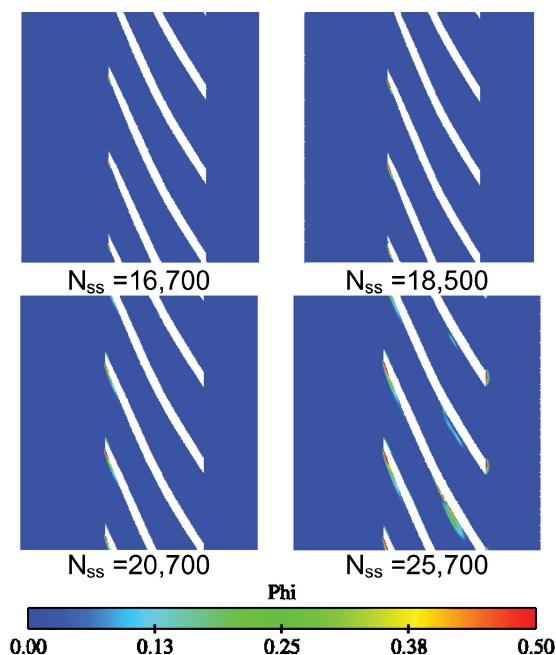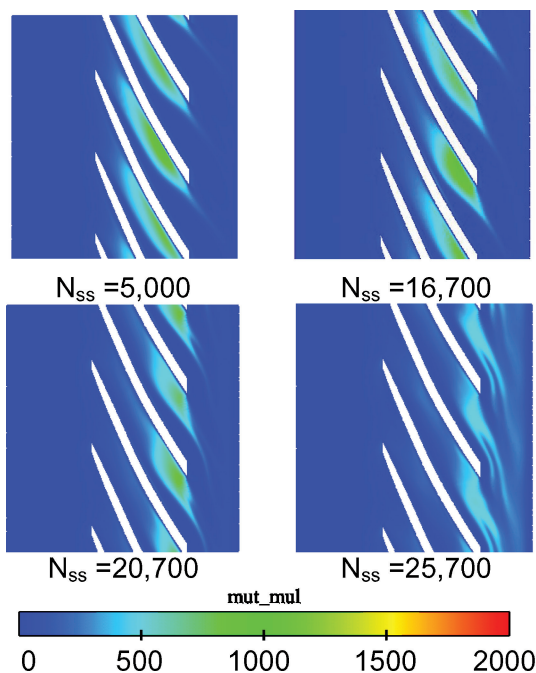
Fig. 11   Cavitation zone at radius = 1.3 in.

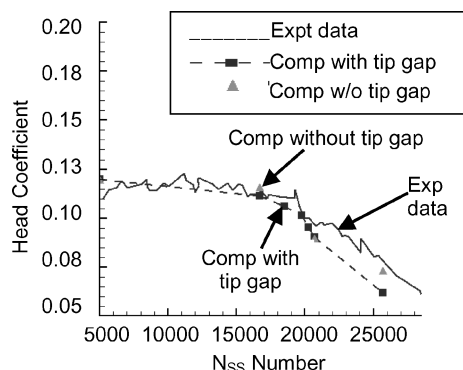**Fig. 12   Turbulent viscosity distribution at radius = 1.3 in.**

Fig. 13   Comparisons of numerical simulations with simplex performance at design flow rate.

suction side rather than the pressure side. Indeed, the large growth of turbulence viscosities near the junction of the blade and the hub indicate that there is a tendency for the flow to stall at this location.

The comparison of the numerically predicted head coefficient vs the experimental value is shown in Fig. 13 as a function of the N_{SS} number at the design flow coefficient. In general good comparison of the head coefficient is obtained over the entire performance range. In particular, the critical N_{SS} number for head breakdown and the change in slope of the inducer performance is simulated very well. The value of the head coefficient itself is slightly lower than the measured value but within an acceptable range of error given the complexity of the problem.

Conclusions

Numerical simulations were performed for the Simplex inducer geometry at the design flow rate of 909 gpm and rpm of 5000 for an inlet tip flow coefficient of 0.094. The numerical analyses were performed at different N_{SS} numbers in the range of 0–30,000. Predictions of head loss compare very well with experimental data. In particular, the numerical simulations predict the breakdown N_{SS} number accurately, and the change in slope of the performance curve in the vicinity of the breakdown N_{SS} number also compares favorably with experimental observations. It is also observed from plots of radial cross sections that the loss in performance directly correlates with the amount of blockage in the blade flow passages caused by cavitation. At the breakdown N_{SS} number, the cavitation zone engulfs the entire blade flow passage close to the shroud and the tip-gap region, thereby dramatically altering the flow. The pressure distribution for N_{SS} numbers below breakdown shows strong fluctuations indicating significant noise caused by highly unsteady cavitation zones. With increasing N_{SS} numbers, the growth in the cavitating zones leads to a stable vapor pocket and reduction in pressure fluctuations. These findings indicate that the present cavitation model and simulation framework accurately capture the effects of performance loss caused by cavitation and provide detailed insights into the flow physics as a consequence of cavitation. Further work will need to be done to investigate and characterize the unsteady cavitation modes and noise.

From a practical perspective, generating multi-element unstructured grids for this inducer that resolves critical flow features with sufficient resolution has proven to be quite straightforward. Run times have also proven to be quite reasonable and should suffice to support most design evaluation studies. In particular, a typical calculation with two million cells run on 32 processors of a Pentium III PC cluster machine can be completed in two days of CPU time.

Acknowledgments

References

[1] Kubota, A., Kato, H., and Yamaguchi, H., "Cavity Flow Predictions Based on the Euler Equations," *Journal of Fluid Mechanics*, Vol. 240, 1992, pp. 59–96.

[2] Colonius, T., d'Auria, F., and Brennen, C. E., "Acoustic Saturation in Bubbly Cavitating Flow Adjacent to an Oscillating Wall," *Physics of Fluids*, Vol. 12, No. 11, 2000, pp. 2752–2761.

[3] Venkateswaran, S., Lindau, J. W., Kunz, R. F., and Merkle, C. L., "Preconditioning Algorithms for the Computation of Multi-Phase Mixture Flows," AIAA Paper 2001-0279, Jan. 2001.

[4] Singhal, A. K., Athavale, M.-M., Li, H., and Jiang, Y., "Mathematical Basis and Validation of the Full Cavitation Model," *Journal of Fluids Engineering*, Vol. 124, Sept. 2002, pp. 617–624.

[5] Ahuja, V., Hosangadi, A., and Arunajatesan, S., "Simulations of Cavitating Flows Using Hybrid Unstructured Meshes," *Journal of Fluids Engineering*, Vol. 123, June 2001, pp. 331–340.

[6] Senocak, I., and Shyy, W., "A Pressure Based Method for Turbulent Cavitating Flow Computations," *Journal of Computational Physics*, Vol. 176, March 2002, pp. 363–383.

[7]Hosangadi, A., Ahuja, V., and Ungewitter, R. J., "Simulations of Cavitating Inducer Flowfields," 38th JANNAF Combustion Subcommittee (CS): Turbomachinery for Space Launch Vehicle Propulsions Systems, April 2002.

[8]Athavale, M. M. and Singhal, A. K., "Numerical Analysis of Cavitating Flows in Rocket Turbopump Elements," AIAA Paper 2001-3400, July 2001.

[9]Dupont, P., and Okamura, T., "Cavitating Flow Calculations in Industry," 9th International Symposium on Transport Phenomena and Dynamics of Rotating Turbomachinery, FD-146, Feb. 2002.

[10]Medvitz, R. B., Kunz, R. F., Boger, D. A., Lindau, J. W., Yocum, A. M., and Pauley, L. L., "Performance Analysis of Cavitating Flow in Centrifugal Pumps Using Multi-Phase CFD," *Journal of Fluids Engineering*, Vol. 124, 2002, pp. 377–383.

[11]Hosangadi, A., Lee, R. A., York, B. J., Sinha, N., and Dash, S. M., "Upwind Unstructured Scheme for Three-Dimensional Combusting Flows," *Journal of Propulsion and Power*, Vol. 12, No. 3, 1996, pp. 494–503.

[12]Hosangadi, A., Lee, R. A., Cavallo, P. A., Sinha, N., and York, B. J., "Hybrid, Viscous, Unstructured Mesh Solver for Propulsive Applications," AIAA Paper 98-3153, July 1998.

[13]Ahuja, V., Shipman, J. D., Arunajatesan, S., and Hosangadi, A., "Multi-Element Unstructured Methodology for Analysis of Turbomachinery Systems" *Journal of Propulsion and Power*, Vol. 19, No. 5, 2003, pp. 945–953.

[14]Bordelon, W., Snellgrove, L., and Zoladz, T., "MSFC Recent and Planned Inducer Water Flow Testing," *Proceedings of TD Fluids Workshop at NASA Marshall Space Flight Center*, April 2001.

[15]Hosangadi, A., and Ahuja, V., "A Generalized Multi-Phase Framework for Modeling Unsteady Cavitation Dynamics and Thermal Effects," AIAA Paper 2003-4000, June 2003.

[16]Merkle, C. L., Feng, J. Z., and Buelow, P. E. O., "Computational Modeling of the Dynamics of Sheet Cavitation," *Proceedings of the 3rd International Symposium on Cavitation*, Grenoble, France, April 1998.

[17]So, R. M. C., Sarkar, A., Gerodimos, G., and Zhang, J., "A Dissipation Rate Equation for Low Reynolds Number and Near-Wall Technique," *Theoretical and Computational Fluid Dynamics*, Vol. 9, Aug. 1997, pp. 47–63.